Investigation of quasi-cleavage in a hydrogen charged maraging stainless steel

Jolan Bestautte, Szilvia Kalácska, Denis Béchet, Zacharie Obadia, Frédéric Christien

Corrosion Science 218 (2023) 111163

Contents lists available at ScienceDirect

Corrosion Science

journal homepage: www.elsevier.com/locate/corsci

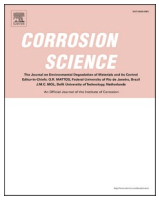

Short communication

Investigation of quasi-cleavage in a hydrogen charged maraging stainless steel

Jolan Bestautte [a], Szilvia Kalácska [a,b,*], Denis Béchet [c], Zacharie Obadia [d], Frederic Christien [a]

[a] Mines Saint-Etienne, Univ Lyon, CNRS, UMR 5307 LGF, Centre SMS, 158 cours Fauriel, 42023 Saint-Étienne, France
[b] Empa, Swiss Federal Laboratories for Materials Science and Technology, Laboratory of Mechanics of Materials and Nanostructures, Feuerwerkerstrasse 39, Thun CH-3602, Switzerland
[c] Aubert & Duval, 63770 Les Ancizes, France
[d] Airbus Commercial Aircraft, Toulouse, France

ARTICLE INFO

Keywords:
Hydrogen embrittlement
Fracture
Maraging steels
Electron backscattering diffraction (EBSD)

ABSTRACT

Slow strain rate tests on hydrogen-containing specimens of PH13–8Mo maraging stainless steel showed H-assisted subcritical quasi-cleavage cracking, accelerating material failure. Fractographic analysis revealed that quasi-cleavage is composed of flat brittle areas and rougher areas. Electron backscatter diffraction (EBSD) was performed on a secondary subcritically grown crack. High resolution EBSD showed significant crystal lattice rotation, hence consequential plastic deformation, concentrated between the main crack tip and the cracks located ahead of it. Quasi-cleavage consisted of {100} cleavage cracks connected by ductile ridges, suggesting a discontinuous mechanism, involving re-initiation of new cleavage cracks ahead the main crack tip.

1. Main text

Lath martensite in steels is a complex microstructure where former austenitic grains are divided in packets of blocks with different orientations [1]. Each block contains several slightly misoriented laths, all belonging to the same martensite variant (or to two slightly misoriented variants in case sub-blocks are present [1]). In most cases, lath or sub-block boundaries are low-angle, whereas block and packet boundaries are high-angle.

Martensitic steels are affected by hydrogen-assisted brittle fracture, that can be either intergranular or "quasi-cleavage" type [2–7]. The term "quasi-cleavage" denotes a fracture mode where fine features, like steps and tear ridges, are present in or between cleavage-like facets [5,8]. According to previous studies, cleavage-like facets in H-charged martensite was shown to propagate along {110} [8–13] or {100} [5,6] lattice planes, the latter being the most expected cleavage plane type in BCC iron [14]. The propagation along {110} planes was interpreted either as a separation along lath boundaries [8,10,13], because those interfaces are usually roughly aligned with the {110} habit plane of martensite, or as glide plane decohesion [11,12].

In a recent study, Cho *et al.* [5] showed that quasi-cleavage in a gaseous hydrogen-embrittled (HE) low alloy martensitic steel was a combination of flat cracks propagating mainly across the laths and along {100} planes, and rugged areas following no particular planes. They also pointed out the crucial role of boundaries in deflecting crack propagation.

The occurrence of subcritical cracking of martensitic steels under hydrogen has been long known [15]. This mechanism designates crack propagation below the intrinsic material toughness. Subcritical crack velocity is usually far below the speed of sound and is governed by time-dependent phenomena occurring at the crack tip [16]. Recent studies [2,17] on maraging steels have demonstrated that hydrogen-assisted brittle fracture during tensile testing can occur through subcritical cracking.

The present study focuses on the PH13–8Mo maraging stainless steel, aged for 4 h at 538 °C. Its yield strength reaches about 1400 MPa thanks to the nanoscale coherent precipitation of NiAl B2 phase [18] inside the martensite laths. A few percent of austenite is also present, mainly as nanometric films covering the different types of boundaries [19]. Slow strain rate testing (SSRT) was performed under or after hydrogen cathodic charging. In contrast to previous works that mainly investigated the main fracture surface [5,8,13], the focus in the current study was set on a secondary crack, *i.e.* not fully propagated across the specimen thickness. This allowed a detailed analysis of the crack tip region at a given instant of the propagation, using conventional electron backscatter diffraction (EBSD) on a cross-section obtained by broad beam ion

* Corresponding author at: Mines Saint-Etienne, Univ Lyon, CNRS, UMR 5307 LGF, Centre SMS, 158 cours Fauriel, 42023 Saint-Étienne, France.
E-mail address: szilvia.kalacska@cnrs.fr (S. Kalácska).

https://doi.org/10.1016/j.corsci.2023.111163
Received 13 December 2022; Received in revised form 21 March 2023; Accepted 3 April 2023
Available online 5 April 2023

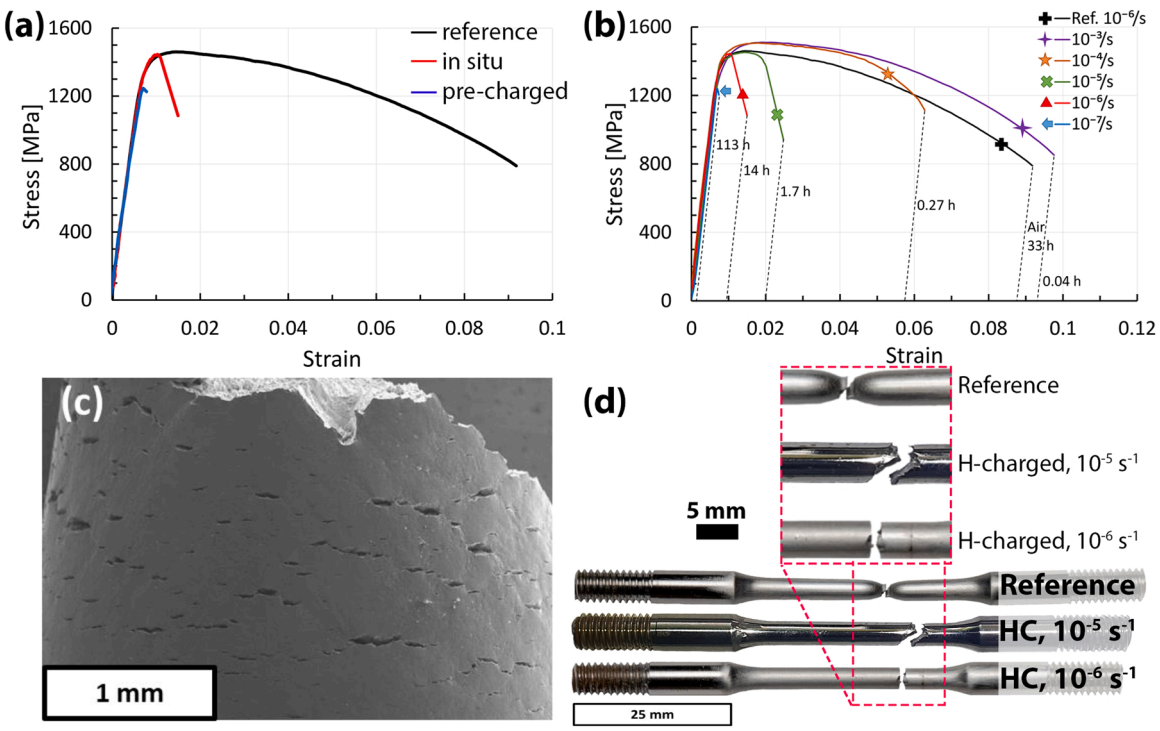

Fig. 1. Tensile test results. (a) Stress-strain curves of PH13–8Mo (10^{-6} s^{-1} strain rate). The results obtained for tensile testing during cathodic charging (*in situ* condition, red curve) and for tensile testing in air after 120 h of cathodic charging (pre-charged condition, blue curve) are compared to the reference test in air (black curve). (b) Influence of the strain rate on stress-strain curves during SSRT (*in situ* conditions). Note that higher flow stresses are observed at 10^{-3} s^{-1} and 10^{-4} s^{-1} experiments under H than at 10^{-6} s^{-1} under air. This is most probably an effect of strain rate rather than an effect of hydrogen. (c) Secondary electron side view of the sample tested at 10^{-4} s^{-1} with *in situ* H-charging, showing considerable secondary cracking. (d) Optical images of the reference and the *in situ* H-charged (HC) samples after SSRT at 10^{-5} s^{-1} and 10^{-6} s^{-1}.

milling. High (angular) resolution EBSD (HR-EBSD) [20,21] evaluation of the local lattice rotation and the dislocation density was also performed.

SSRT was carried out at multiple strain rates (10^{-7} – 10^{-3} s^{-1}). Two H-charging methods were evaluated using i) samples that were charged during the tensile testing (referred to as "*in situ*") and ii) specimens that were pre-charged during 120 h before deformation in air. More information about the charging and mechanical testing can be found in the Supplementary Materials. An additional fracture toughness test was conducted in air following the ASTM E399 standard under predominantly linear-elastic, plane-strain conditions. A Compact Tension (CT) specimen of type CT20 was used after fatigue pre-cracking. The aim of this experiment was to obtain a fracture surface resulting from critical cracking under air to serve as a reference for comparison to the fracture surfaces obtained after SSRT under hydrogen. The fracture toughness obtained in air was 87 MPa $m^{1/2}$.

Stress-strain ($\sigma - \varepsilon$) curves obtained at 10^{-6} s^{-1} are shown in Fig. 1a. The yield strength and elongation at fracture for the reference specimen tested in air are ~1400 MPa and 9%, respectively. It should be noted that the material shows very limited work hardening, as the ultimate tensile strength does not exceed 1430 MPa. The optical image of the reference sample after fracture (Fig. 1d) reveals significant necking, which is consistent with the progressive reduction in load visible on the tensile curve (black curve in Fig. 1a and b).

Fig. 1a shows considerable reduction of the elongation at fracture at 10^{-6} s^{-1} due to hydrogen in both *in situ* and pre-charged conditions. The optical image of the *in situ* H-charged sample after fracture (Fig. 1d) reveals no necking at all. The strain rate sensitivity of the *in situ* H-charged material was further investigated. In Fig. 1b, several *in situ* $\sigma - \varepsilon$ curves are simultaneously plotted, including the reference curve deformed at 10^{-6} s^{-1} in air. The sensitivity to hydrogen embrittlement is shown to increase significantly with decreasing strain rate. Only at the strain rate of 10^{-3} s^{-1}, the H-charged sample could sustain similar elongation as the reference before failure. Significant necking, visible in Fig. 1c, was obtained at 10^{-4} s^{-1}. In contrast, no necking was observed at 10^{-5} and 10^{-6} s^{-1} (Fig. 1d), meaning that the material behaved purely in a brittle manner at the macroscale. The progressive reduction in the load visible on the tensile curves for the slowest strain rates is therefore not related to ductile necking. This supports the existence of subcritical cracking in the tensile specimens due to hydrogen. Fig. 1c is a side view of the specimen tested in *in situ* H-charging conditions at 10^{-4} s^{-1}, where a considerable number of secondary cracks are visible on the surface. This confirms the existence of H-assisted subcritical cracking, as already observed in similar materials in previous studies [2,4].

Fig. 2 shows the fractographic observations conducted on the sample tested *in situ* at 10^{-6} s^{-1}. The overall fracture surface can be divided into three distinct regions. In the region closest to the edge of the sample, the crack presents a quasi-cleavage (QC) morphology (red area in Fig. 2a). The QC surface (Fig. 2d) consists of flat facets with river patterns and of other rougher areas. Fig. 2e is a higher magnification image of two flat facets (marked with white flags), clearly showing some river patterns, surrounded by rougher areas.

The second part of the crack corresponds to the green area in Fig. 2a and it is located deeper in the sample. The fracture surface in this part of the crack appears to be different from the QC region, including more curved and embossed patterns (Fig. 2b). The existence of small dimples is presented in Fig. 2c, that are not apparent in the QC region. Moreover, cleavage rivers are hardly ever observed in this inner part of the crack. Therefore, due to the more ductile aspect, we refer to this crack morphology as ductile cracking (DC). For comparison, Fig. 3 shows the fracture surface obtained through critical cracking of a pre-cracked CT specimen tested in air. The fracture surface obtained is similar to that of Fig. 2(b) and (c), suggesting that the green area in Fig. 2 is also obtained from critical cracking.

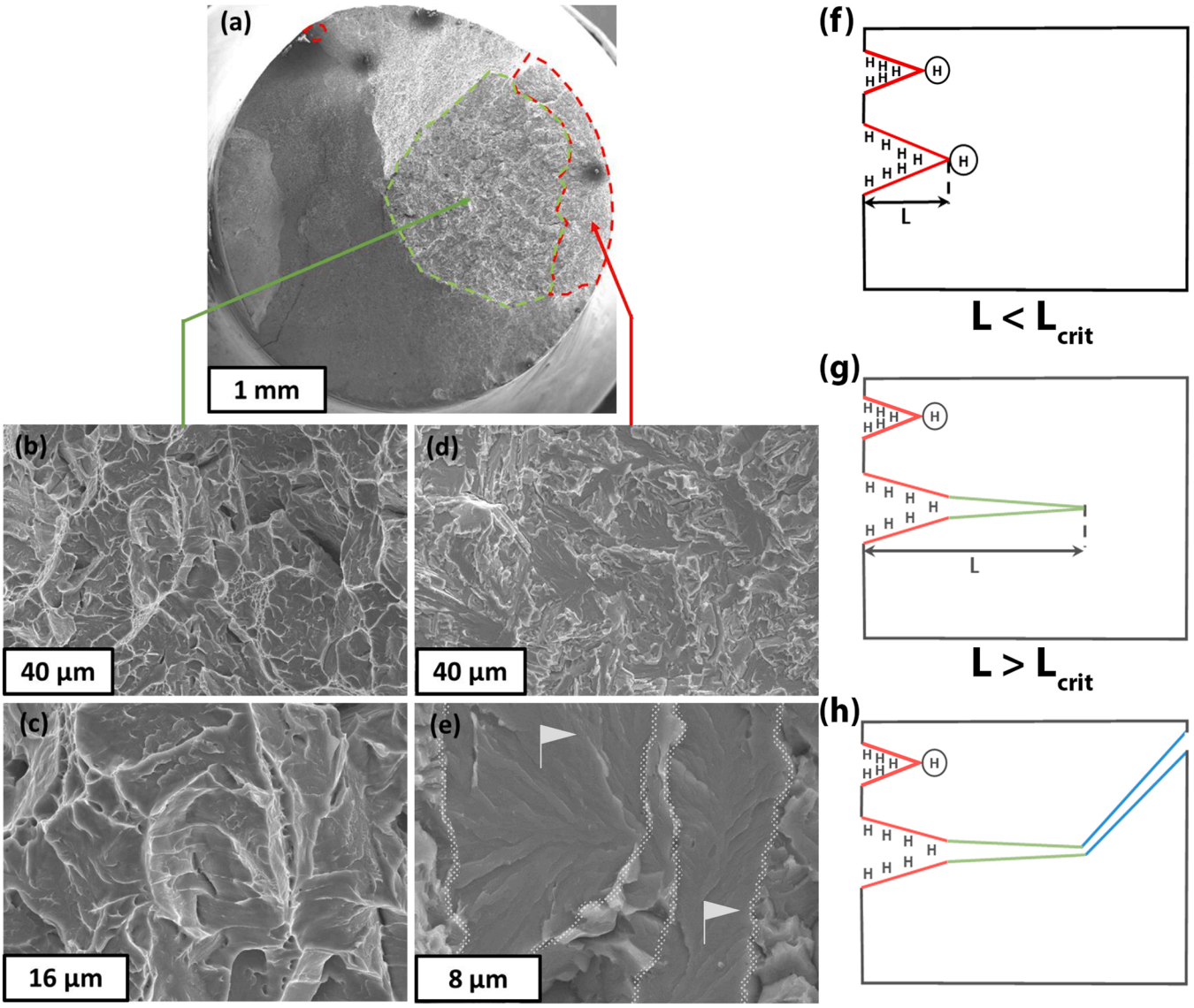

Fig. 2. Fracture surface morphologies. (a) Fracture surface of the sample tested *in situ* at 10^{-6} s^{-1}. The green region corresponds to ductile cracking (DC), associated with critical cracking. Higher magnification pictures of the DC region are presented in (b) and (c). The red region corresponds to quasi-cleavage (QC) cracking, associated with subcritical cracking. Higher magnification pictures of the QC region are presented in (d) and (e). The rest of the fracture surface is composed of shear lips. (f-h) Schematic representation of the sequence leading to the failure of a SSRT specimen in *in situ* H-charging condition. (f) Slow propagation of a subcritical crack assisted by hydrogen, which is adsorbed on crack surfaces and accumulates ahead of the crack tip. (g) Fast propagation of a critical crack after the subcritical crack reaches a critical length L_{crit}. The high crack growth rate most probably prevents any hydrogen/crack interaction. (h) Shearing leading to the final failure of the sample.

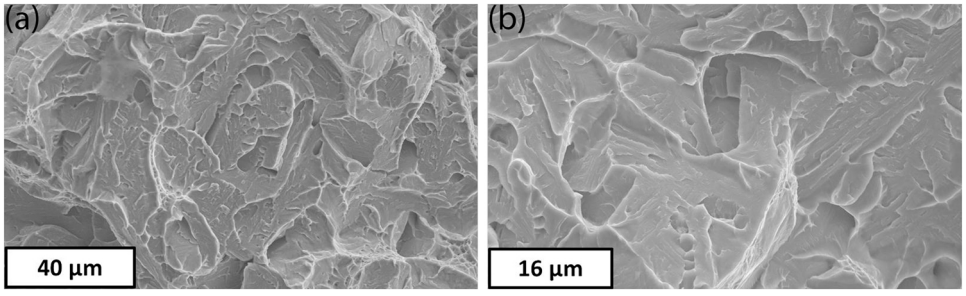

Fig. 3. Fracture surface morphologies of the pre-cracked CT specimen tested in air at (a) lower and (b) higher magnification. The crack morphology observed here corresponds to critical cracking.

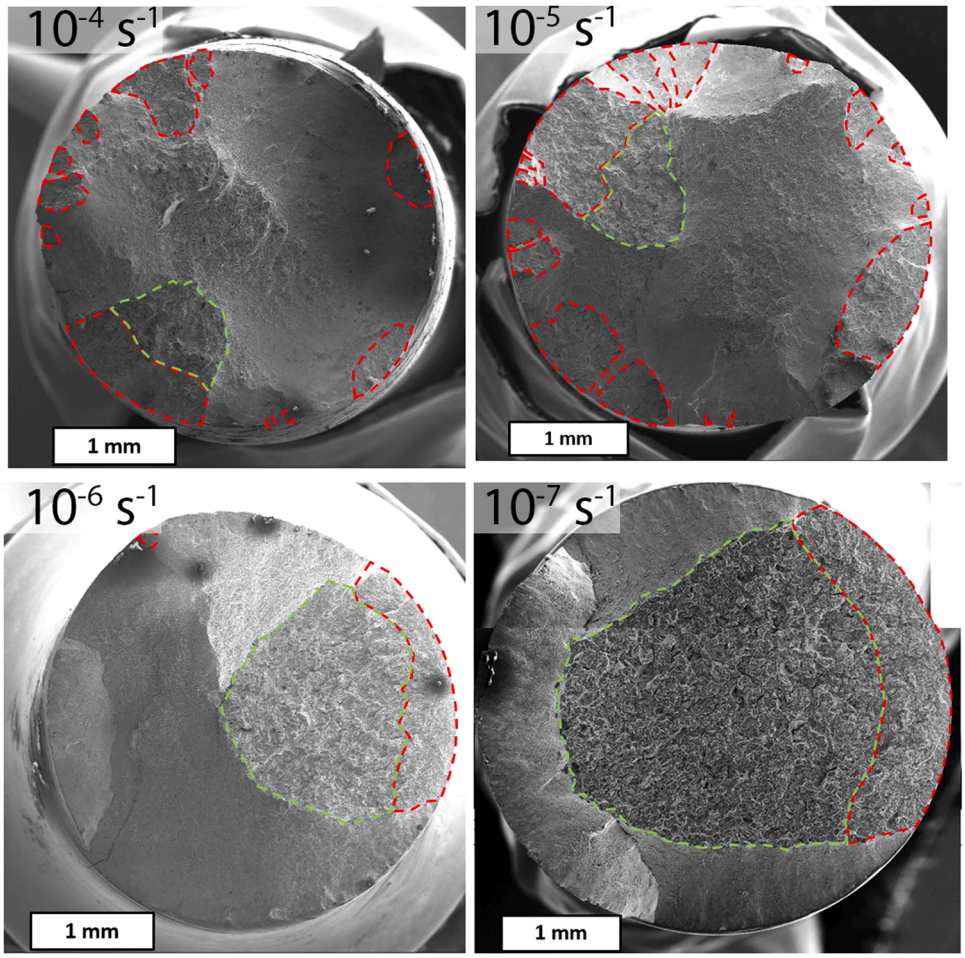

Fig. 4. Fracture surfaces of the specimens tested *in situ* at strain rates ranging between 10^{-4} and 10^{-7} s^{-1}. Red dashed lines surround the areas of subcritical cracking. Green areas correspond to DC critical cracking.

Looking at the morphologies of fracture surfaces obtained at a strain rate of ~10^{-6} s^{-1} (Fig. 2a-e), the following hypothesis can be made on the sequence that led to the failure of the sample. At the first stage (Fig. 2f), hydrogen-assisted cracks initiated and propagated subcritically under the effect of hydrogen towards the centre of the sample, following a QC propagation mode. Once a subcritical crack has propagated to a certain extent, stress triaxiality locally increases a lot. Similar to the case of pre cracked CT specimens, this situation favours the critical propagation of a ductile crack, rather than extended plastic deformation and necking. So in the second stage (Fig. 2g), one of the QC cracks reached a critical length for which the stress intensity factor at the crack tip exceeded the fracture toughness value of the material. Consequently, the crack propagation shifted from subcritical to critical. The critical crack propagated at a very high rate, which leaves insufficient time for any hydrogen to diffuse and allow embrittlement to take place. This critical crack propagation is therefore most probably uncorrelated with the presence of hydrogen and corresponds to the DC morphology. In a third stage (Fig. 2h), the final failure of the sample was obtained by shearing of the remaining ligament, corresponding to the shear lips on the fracture surface.

Fig. 4 compares the overall fracture surfaces of the tensile specimens tested under *in situ* H charging at strain rates between 10^{-4} and 10^{-7} s^{-1}, where the subcritical cracks are circled in red. It can be noticed that the subcritical crack depth is roughly about the same in all the specimens, which means that it does not significantly depend on the strain rate. This can be interpreted as the result of the transition from subcritical to critical cracking when the stress intensity factor of the growing subcritical cracks reaches the intrinsic material's fracture toughness (87 MPa $m^{1/2}$). The stress intensity factor K is given by:

$$K = Y\sigma\sqrt{\pi a} \tag{1}$$

where Y is the geometry factor, σ is the stress and a is the crack depth. Considering for example the tensile test at 10^{-7} s^{-1}, where a single subcritical crack of depth $a \approx 600$ μm is visible on the fracture surface (Fig. 4), and the final fracture stress is about 1200 MPa (Fig. 1b), Eq. 1 gives a geometry factor $Y = 1.7$, which is consistent considering the shape of the subcritical crack (much elongated in the circumferential direction).

According to the scenario proposed in Fig. 2f-h, all the secondary cracks have grown subcritically but did not transition into critical cracks. It is then expected that secondary cracks consist of quasi-cleavage only. In order to investigate quasi-cleavage, a cross-section of a secondary crack was prepared. For that purpose, the sample tested at 10^{-5} s^{-1} with *in situ* H-charging was selected, as it showed significant secondary cracking, with no (or limited) generalized plasticity that could interfere with the EBSD measurements. More details about the sample preparation and the cross-section method can be found in the Suppl. Materials.

Fig. 5a-c shows the secondary electron observations and the EBSD analysis of the crack tip region. The tensile axis corresponds to the vertical direction. Note that only the crack tip region (located at about 450 μm from the specimen edge) was studied. The crack has a segmented aspect and shows many bifurcations (Fig. 5a). It is noticeable that two small cracks (α and β) are present ahead of the main crack tip. These two cracks are apparently disconnected from the main crack

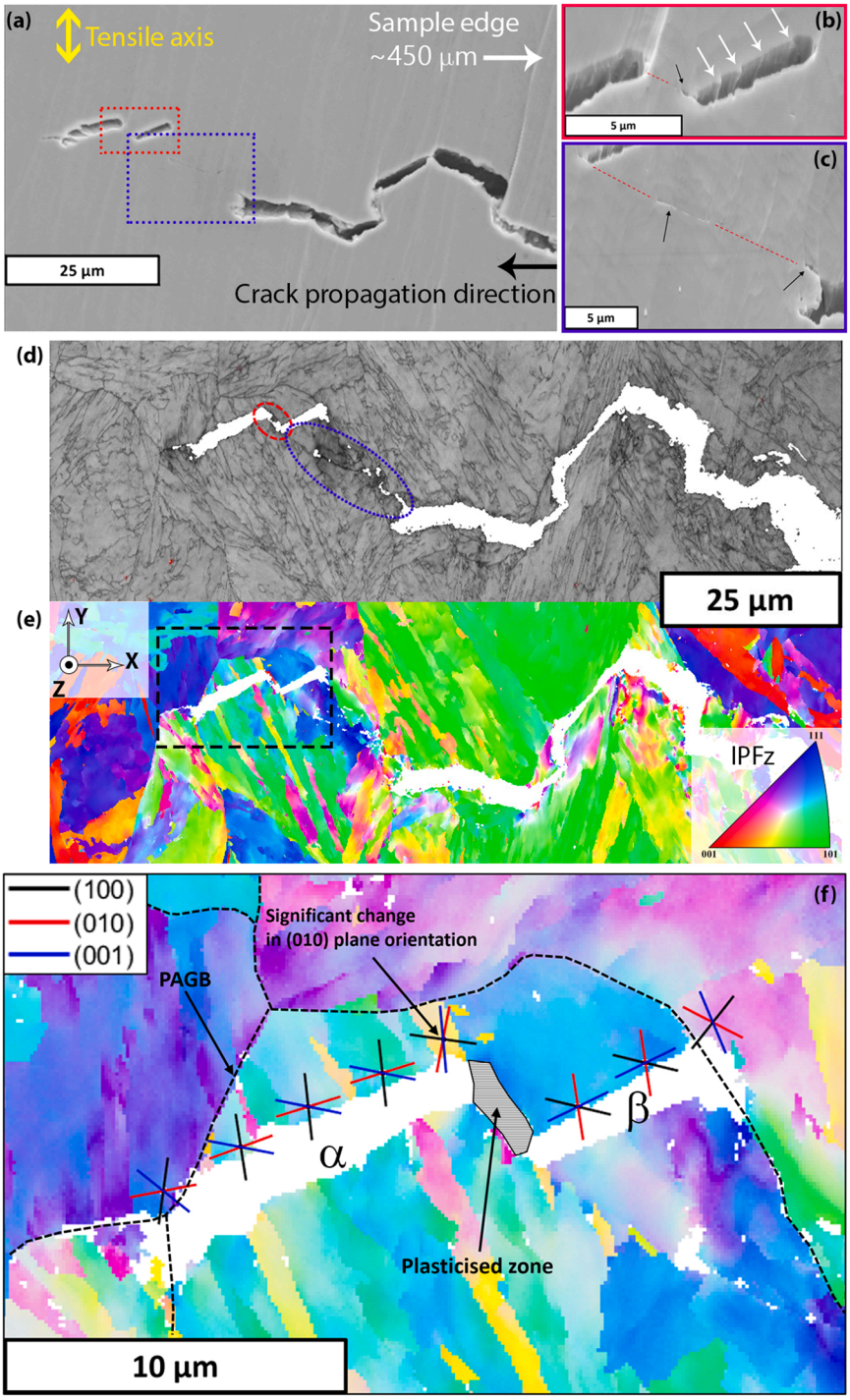

Fig. 5. EBSD results. (a) Cross-sectional scanning electron micrograph of the secondary crack obtained *in situ* at 10^{-5} s^{-1}. (b) Higher magnification of the two internal cracks. (c) Higher magnification of the ligament between the main crack tip and one of the internal cracks. (d) EBSD band contrast map. Low-indexation plasticised zones are highlighted with circles. (e) The corresponding IPF map. (f) Higher magnification IPF map corresponding to the area indicated in (e) with a black dashed rectangle. The traces of {100} type planes are indicated as well as the presence of plasticised zone.

(however since we can only get information from a 2D section of a 3D fracture structure, the discontinuity cannot be fully supported by one measurement). The two small cracks are separated by a small, uncracked ligament. Each of these two cracks is relatively straight (no bifurcation is present). However, steps are clearly visible in Fig. 5b on the cracked surfaces (highlighted by white arrows). Defects are observed (black arrows) between the two small cracks (Fig. 5b) and in the uncracked ligament separating the two small cracks from the main crack tip (Fig. 5c). Furthermore, the latter area appears darker in the EBSD band contrast map (Fig. 5d), which is a first indication of locally intense plastic deformation.

The band contrast and inverse pole figure (IPF) maps shown in Fig. 5d and e show that the cracks are transgranular, *i.e.* they do not seem to follow prior austenite grain boundaries (PAGBs), or any other type of boundaries. Fig. 5f is a higher magnification IPF map focusing on the two small cracks located ahead of the main crack tip. The dotted lines show the PAGBs. Each crack goes through *one entire* martensite block. In other words, the cracks stop at PAGBs or block boundaries. A highly plasticized zone is present between the two cracks, where EBSD indexation rate was found to be lower. To assess if those cracks follow a specific crystallographic plane, the traces of {100} type planes are shown. Traces of {110}-type planes are also shown in Suppl. Fig. S4. The crack directions observed here are consistent with a propagation along {100} type planes. Suppl. Fig. S5 and S6 show complementary trace

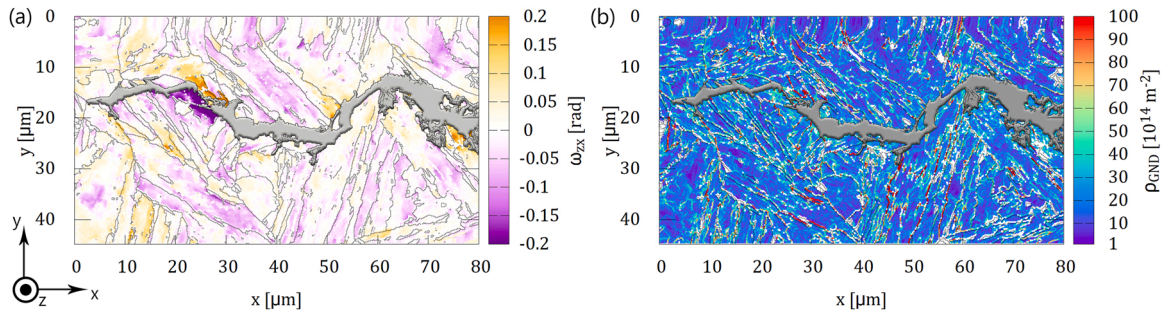

Fig. 6. HR-EBSD results. (a) ω_{zx} rotation tensor and (b) GND density map. Black lines highlight the high-angle grain boundaries (misorientation >10°).

analysis of a secondary internal crack extracted from a pre-charged specimen tested at 10^{-5} s^{-1}.

Fig. 5d suggests intense plastic deformation concentrated between cracks. To study these plastic zones, HR-EBSD was applied to calculate the lattice rotation tensor elements (ω_{ij}) and geometrically necessary dislocation (GND) density (ρ_{GND}) using the BLGVantage CrossCourt v4.0 software (Fig. 6). HR-EBSD is an image cross-correlation technique utilized on the raw EBSD patterns [20], where a reference diffraction pattern is chosen at each grain to relate the state of each other pixel within that grain to this point. The results given by this technique are therefore relative to the reference patterns that should ideally be selected at the minimal / zero stress state. In the absence of such references in our sample, HR-EBSD provides only a relative / qualitative support to the microstructure analysis to highlight the increased plastic zones around the cracks. More information about the HR-EBSD experiments are provided in the Suppl. Materials.

Increased ω_{zx} values (Fig. 6a) were found around the plasticised zone located between the main crack and the two internal cracks, indicating large lattice rotations in this area. This confirms the local intense plastic activity suggested by the band contrast map of Fig. 5d. The concentration of plastic deformation between the cracks suggests that this plastic deformation results from the mechanical interaction between cracks under tensile loading. This would imply that the cracks were formed first and the locally intense plastic deformation occurred later. Further components of the ω_{ij} tensor can be seen in Suppl. Fig. S7.

The estimated ρ_{GND} map (Fig. 6b) shows an overall high dislocation density (of the order of 10^{15} m^{-2}), comparable to other measurements in similar materials [22,23]. The dislocations are mainly concentrated along lath boundaries, typical to martensitic steels [22]. On the other hand, no significant local increase of the dislocation density is measured in the plasticized zone located between the cracks. This can be related to the quasi-absence of work-hardening in this material, where plastic deformation is obtained from movements of the already existing dislocations, rather than by dislocation multiplication.

The investigations conducted here suggest a discontinuous mechanism of hydrogen-assisted subcritical quasi-cleavage cracking, rather than a continuous propagation of the crack. High-angle grain boundaries are efficient obstacles to the crack propagation. These observations suggest that once the main crack tip is stopped at a high-angle boundary, new cleavage cracks of the size of one martensite block can form some micrometres (or even tens of micrometers) ahead of the main crack tip. This is possible most probably because of the high hydrostatic stress around the crack tip, that concentrates hydrogen there (note that the maximum hydrostatic stress is located at some distance ahead the crack tip, depending on the crack geometry). Once a new cleavage crack has formed, intense plastic deformation takes place in the ligament located between the main crack tip and the newly formed cleavage crack, until ductile failure of the ligament. In this mechanism, the local ductile failure is not expected to follow any particular crystallographic plane, as it is mainly governed by the stress field between the cracks. Once the newly formed cleavage cracks are connected to the main crack, the process can further repeat itself. The effect of hydrogen in this mechanism is of course expected in facilitating the formation of cleavage cracks, but it may also play a significant role in the failure of ductile connections.

Given this mechanism, quasi-cleavage in the material investigated here can be rationalised as a discontinuous process involving i) actual cleavage cracks propagated along {100} type planes across single martensite blocks, and ii) ductile connections between cleavage cracks. This leads to the aspect of quasi-cleavage shown in Figs. 2d and 2e, where flat and rougher areas correspond to cleavage facets and ductile connections, respectively.

CRediT authorship contribution statement

Jolan Bestautte: Methodology, Validation, Formal analysis, Writing – original draft. **Szilvia Kalácska:** Methodology, Validation, Formal analysis, Writing – original draft, Writing – review & editing. **Denis Béchet:** Methodology, Writing - original draft. **Zacharie Obadia:** Methodology, Writing - original draft. **Frederic Christien:** Conceptualization, Methodology, Validation, Supervision, Project administration, Writing - original draft, Writing - review & editing.

Declaration of Competing Interest

The authors declare that they have no known competing financial interests or personal relationships that could have appeared to influence the work reported in this paper.

Data Availability

Data will be made available on request.

Acknowledgements

This research was mainly funded by Aubert & Duval and Airbus, with the support of ANRT (Association Nationale de la Recherche et de la Technologie).

Fruitful discussions in the CASHMERE R&T consortium (Airbus, Aubert & Duval, University of Manchester, Mines Saint-Etienne, La Rochelle University and French Corrosion Institute) are acknowledged, as well as the material supplied by Aubert & Duval.

The authors wish to express their sincere thanks to Claire Roume and Marilyne Mondon (Mines Saint-Etienne) for their technical support in this study.

Appendix A. Supporting information

Supplementary data associated with this article can be found in the online version at doi:10.1016/j.corsci.2023.111163.

References

[1] S. Morito, X. Huang, T. Furuhara, T. Maki, N. Hansen, The morphology and crystallography of lath martensite in alloy steels, Acta Mater. 54 (2006) 5323–5331, https://doi.org/10.1016/j.actamat.2006.07.009.

[2] M. Alnajjar, F. Christien, C. Bosch, K. Wolski, A comparative study of microstructure and hydrogen embrittlement of selective laser melted and wrought 17–4 PH stainless steel, Mater. Sci. Eng. A. 785 (2020), 139363, https://doi.org/10.1016/j.msea.2020.139363.

[3] G. Wang, Y. Yan, J. Li, J. Huang, L. Qiao, A.A. Volinsky, Microstructure effect on hydrogen-induced cracking in TM210 maraging steel, Mater. Sci. Eng. A 586 (2013) 142–148, https://doi.org/10.1016/j.msea.2013.07.097.

[4] Z. Yang, Z. Liu, J. Liang, J. Su, Z. Yang, B. Zhang, G. Sheng, Correlation between the microstructure and hydrogen embrittlement resistance in a precipitation-hardened martensitic stainless steel, Corros. Sci. 182 (2021), 109260, https://doi.org/10.1016/j.corsci.2021.109260.

[5] L. Cho, P.E. Bradley, D.S. Lauria, M.L. Martin, M.J. Connolly, J.T. Benzing, E.J. Seo, K.O. Findley, J.G. Speer, A.J. Slifka, Characteristics and mechanisms of hydrogen-induced quasi-cleavage fracture of lath martensitic steel, Acta Mater. 206 (2021), 116635, https://doi.org/10.1016/j.actamat.2021.116635.

[6] C.D. Beachem, Orientation of cleavage facets in tempered martensite (quasi-cleavage) by single surface trace analysis, Metall. Trans. 4 (1973) 1999–2000, https://doi.org/10.1007/BF02665434.

[7] X. Li, J. Zhang, E. Akiyama, Q. Li, Y. Wang, Effect of heat treatment on hydrogen-assisted fracture behavior of PH13-8Mo steel, Corros. Sci. 128 (2017) 198–212, https://doi.org/10.1016/j.corsci.2017.09.018.

[8] A. Nagao, C.D. Smith, M. Dadfarnia, P. Sofronis, I.M. Robertson, The role of hydrogen in hydrogen embrittlement fracture of lath martensitic steel, Acta Mater. 60 (2012) 5182–5189, https://doi.org/10.1016/j.actamat.2012.06.040.

[9] G. Ming, R.P. Wei, Quasi-cleavage and martensite habit plane, Acta Met. 32 (1984) 2115–2124, https://doi.org/10.1016/0001-6160(84)90190-1.

[10] Y.H. Kim, J.W. Morris, The nature of quasicleavage fracture in tempered 5.5Ni steel after hydrogen charging, Metall. Trans. A 14 (1983) 1883–1888, https://doi.org/10.1007/BF02645559.

[11] A. Shibata, T. Murata, H. Takahashi, T. Matsuoka, N. Tsuji, Characterization of hydrogen-related fracture behavior in as-quenched low-carbon martensitic steel and tempered medium-carbon martensitic steel, Metall. Mater. Trans. A 46 (2015) 5685–5696, https://doi.org/10.1007/s11661-015-3176-x.

[12] A. Shibata, Y. Momotani, T. Murata, T. Matsuoka, M. Tsuboi, N. Tsuji, Microstructural and crystallographic features of hydrogen-related fracture in lath martensitic steels, Mater. Sci. Technol. 33 (2017) 1524–1532, https://doi.org/10.1080/02670836.2017.1312210.

[13] D. Guedes, L. Cupertino Malheiros, A. Oudriss, S. Cohendoz, J. Bouhattate, J. Creus, F. Thébault, M. Piette, X. Feaugas, The role of plasticity and hydrogen flux in the fracture of a tempered martensitic steel: a new design of mechanical test until fracture to separate the influence of mobile from deeply trapped hydrogen, Acta Mater. 186 (2020) 133–148, https://doi.org/10.1016/j.actamat.2019.12.045.

[14] G.E. Dieter, D.J. Bacon, Mechanical Metallurgy, McGraw-Hill, London; New York, 1988.

[15] R.P. Gangloff, R.P. Wei, Gaseous hydrogen embrittlement of high strength steels, Metall. Trans. A 8 (1977) 1043–1053, https://doi.org/10.1007/BF02667388.

[16] B. Tomkins, H.K. Grover, T.G.F. Gray, Subcritical crack growth: fatigue, creep and stress corrosion cracking, Philos. Trans. R. Soc. Lond. A 299 (1981) 31–44.

[17] A. Dreano, M. Alnajjar, F. Salvatore, J. Rech, C. Bosch, K. Wolski, G. Kermouche, F. Christien, Effect of ball-burnishing on hydrogen-assisted cracking of a martensitic stainless steel, Int. J. Hydr. Energy 47 (93) (2022) 39654–39665, https://doi.org/10.1016/j.ijhydene.2022.09.110.

[18] S. Jiang, H. Wang, Y. Wu, X. Liu, H. Chen, M. Yao, B. Gault, D. Ponge, D. Raabe, A. Hirata, M. Chen, Y. Wang, Z. Lu, Ultrastrong steel via minimal lattice misfit and high-density nanoprecipitation, Nature 544 (2017) 460–464, https://doi.org/10.1038/nature22032.

[19] R. Schnitzer, R. Radis, M. Nöhrer, M. Schober, R. Hochfellner, S. Zinner, E. Povoden-Karadeniz, E. Kozeschnik, H. Leitner, Reverted austenite in PH 13-8 Mo maraging steels, Mater. Chem. Phys. 122 (2010) 138–145, https://doi.org/10.1016/j.matchemphys.2010.02.058.

[20] A.J. Wilkinson, G. Meaden, D.J. Dingley, High-resolution elastic strain measurement from electron backscatter diffraction patterns: new levels of sensitivity, Ultra 106 (4–5) (2006) 307–313, https://doi.org/10.1016/j.ultramic.2005.10.001.

[21] S. Kalácska, J. Ast, P.D. Ispánovity, J. Michler, X. Maeder, 3D HR-EBSD Characterization of the plastic zone around crack tips in tungsten single crystals at the micron scale, Acta Mater. 200 (2020) 211–222, https://doi.org/10.1016/j.actamat.2020.09.009.

[22] X. Li, S.R. Holdsworth, S. Kalácska, L. Balogh, J.-S. Park, A.S. Sologubenko, X. Maeder, S. Kabra, E. Mazza, E. Hosseini, Primary creep regeneration in 10% Cr martensitic steel: in-situ and ex-situ microstructure studies, Mater. Des. 199 (2021), 109405, https://doi.org/10.1016/j.matdes.2020.109405.

[23] F. Christien, M.T.F. Telling, K.S. Knight, Neutron diffraction in situ monitoring of the dislocation density during martensitic transformation in a stainless steel, Scr. Mater. 68 (7) (2013) 506–509, https://doi.org/10.1016/j.scriptamat.2012.11.031.